WAX DEPOSITION MODEL ANALYSIS

Arya Shahdi, Moldir Yermekova, Ekarit Panacharoensawad
Texas Tech University

ABSTRACT

Wax deposition in subsea and offshore pipeline is one of the significant current flow assurance problems. There are several wax deposition models proposed in the literatures. However, all of them are validated based on the limited number of data and have not been crosschecked with other researchers' data. All of wax deposition model on turbulent flow contain the unknown physical parameters which required in wax deposition prediction. Nevertheless, the closure relationship of the unknown parameters are not provided and these available models cannot be used as self-sufficient predictive tools. This work provides the performance analysis of wax deposition models by testing the proposed model (such as Singh et al.[1]) against the experimental data that are just recently available. The contribution of this work is the understanding in the uncertainty and the limitation in wax deposition model currently available in several commercial software.

INTRODUCTION

Crude oil includes saturates, aromatics, asphaltenes and resins.[2] Among mentioned constituents, components with high molecular weight (paraffin and asphaltene) are, normally, responsible for production and transportation difficulties.[3] As they are completely soluble in the oil phase under reservoir conditions (70-150 $°C$ and 50-100 MPa),[4] the main focus is on their transportation. Specifically, wax/paraffin becomes problematic as the petroleum fluid flows through a subsea pipeline laying on the ocean floor at a temperature considerably less than the reservoir temperature.[5]

Cloud point (or wax appearance temperature WAT) is the temperature that wax crystals start to precipitate. Normally, oil is transported through a pipeline with surrounding temperature of $5°C$. Due to heat lost, the oil temperature drops to a point that is less than WAT causing the formation of wax deposition on the pipe wall.[6] Singh et al[1] proposed that wax deposits in the form of wax-oil gels on the pipe wall. The mentioned waxy film reduces the effective radius for the fluid to flow and its further growth can cause the complete blockage of the pipe. Ultimate remediation is to stop the production and change the blocked pipe. The magnitude of financial harm could be as high as $100 million mainly because of abandonment of the platform and production.[1] Since oil reservoirs in the shallow parts near shoreline have been depleted, oil production in deep sea areas have been financially profitable and has increased significantly.[4] It has been approximated, by the year of 2017, the oil production from deep sea areas will be more than 8 million barrels per day.[7] As more oil is produced from deep water areas and transportation lines become longer due to their extended distances from shoreline, wax/paraffin related problems become more severe. Each remedial action such as cutting and replacing the subsea pipeline is extremely expensive. Pigging the pipeline can also be costly, too. Therefore, the pigging frequency should be determined optimally. Prior to Singh et al.[1] publication, a number of mathematical models based on the assumption that wax-oil deposits have a constant deposit wax fraction have been introduced.[8–11] The pipeline pigging frequency is dependent upon the deposit strength which as mainly controlled by the deposit thickness and the deposit wax fraction.[12] Therefore, comprehensive modeling approaches, based on heat and mass transfer, have been proposed. Yet, the experimental data used for the model validation part is limited. Examples of these transport equations based models are Singh et al,[1] Venkatesan,[3] Lee,[4] Huang et al,[13] and Panacharoensawad[14].

All of the proposed models have parameters that are not independently defined and need to be manually chosen in order to fit the predicted data with the experimental data. These limiting factors hinder current models from predicting the thickness and solid wax fraction independently without having to fit them with the experimental data. Therefore, more research is required to investigate on the factors that are potentially responsible for any change in the limiting factors. In this study, these limiting factors are analyzed and their dependences on different elements have been investigated. Moreover, the defined factors with known equations can be dependent upon the numerical method applied in the model. The improvement on numerical method implementation has been completed to have a consistency of the heat and mass balance updating within the RK4 calculation steps. This study targets the mentioned equations and a modified numerical approach and shows the effect on waxy gel thickness and its solid wax fraction. Also, an equation has been derived step by step using available mass/heat transfer correlations to back calculate wax crystal aspect ratio. In wax mass flux analysis, Rittirong[15] has proposed an equation with uncertainty that, in this paper, it was approached differently and proven to be valid.

2 LIMITING FACTORS

Different modeling approaches have been proposed for laminar and turbulent flow regimes and each of them has different limiting factors. Therefore, this section in divided into two flow regimes to independently elaborate the limiting factors for each case.

2.1 Laminar Flow

The total mass deposit formed on the cold pipe wall is as follows:

$$M = \pi(R^2 - r_i^2)\Delta L \rho_{dep} \bar{F}_w \quad \text{..... (1)}$$

$$\frac{dM}{dt} = \underbrace{\frac{\partial M}{\partial \bar{F}_w}\frac{d\bar{F}_w}{dt}}_{aging} + \underbrace{\frac{\partial M}{\partial r_i}\frac{dr_i}{dt}}_{growth} \quad \text{..... (2)}$$

Total Wax Mass Flux:

$$q_{M,IN} = q_{M,Aging} + q_{M,Growth} \quad \text{..... (3)}$$

Also:

$$2\pi r_i \Delta L \cdot q_{M,Aging} = \frac{\partial M}{\partial \bar{F}_w}\frac{d\bar{F}_w}{dt},\ q_{M,Aging} = -D_e \frac{\partial C}{\partial r}\Big|_{r_i^+} \quad \text{..... (4), (5)}$$

$$2\pi r_i \Delta L \cdot q_{M,IN} = \frac{\partial M}{\partial t},\ q_{M,IN} \equiv k_M(C_b - C_{ws}) \quad \text{..... (6), (7)}$$

$$2\pi r_i \Delta L \cdot q_{M,Growth} = \frac{\partial M}{\partial r_i}\frac{dr_i}{dt} \quad \text{..... (8)}$$

Then, the waxy gel thickness and its solid wax fraction can be calculated from the following governing equations[1]:

$$\frac{d\bar{F}_w}{dt} = \frac{-2r_i D_e \frac{\partial C}{\partial r}\Big|_{r_i^+}}{(R^2 - r_i^2)\rho_{oil}} \quad \text{..... (9)}$$

$$-\frac{dr_i}{dt} = \frac{k_M(C_b - C_{ws}) + D_e \frac{\partial C}{\partial r}\Big|_{r_i^+}}{\bar{F}_w \rho_{oil}} \quad \text{..... (10)}$$

where, $\bar{F}_w$ is the solid wax fraction in the deposition, ρ_{dep} is the density of the wax deposit, k_M is the inner convective mass transfer coefficient, C_b is the bulk concentration of wax molecules, C_{ws} is the concentration of wax molecule at the interface, R is the radius of a pipe, ΔL is the length of the test section, D_e is the effective diffusivity in the deposit as given by Cussler et al.[16] The effective diffusivity was calculated from Cussler et al[16] (11) which is based on slits model (Figure 8) and in the corresponding equation, the wax crystal aspect ratio was defined as the fraction of length and width of wax crystals. However the actual gel structure is a three dimensional network of wax particles.[17]

$$D_e = \frac{D_{wo}}{1 + \alpha^2 \bar{F}_w^2/(1 - \bar{F}_w)} \quad \text{..... (11)}$$

$$\alpha = k_\alpha \bar{F}_w + 1 \quad \text{..... (12)}$$

where, α is the aspect ratio of the wax crystals in the deposit (width to thickness), D_{wo} is molecular diffusivity of wax in oil as given by Hayduk and Minhas,[18] k_α is an adjustable parameter.

As it can be seen in the governing equations, effective radius and solid wax fraction are interdependent and will vary as the other one changes. Notably, D_e (effective diffusivity) exists in both of the mentioned equations which shows extra criticality. This parameter helps to mathematically explain the proposed counterdiffusion phenomena as wax molecules enter the 3D network of wax crystals.[19] This element is dependent upon wax crystal aspect ratio and α itself is a function of k_α and $\bar{F}_w$.

2.2 Turbulent Flow

In order to obtain the wax deposition thickness and its solid wax fraction, the inner convective heat and mass transfer coefficient, h_i and $k_M$need to be calculated.[20]

$$Nu = \frac{hD}{k} = -\frac{D}{T_b - T_i}\frac{\partial T}{\partial r}\Big|_{r=r_i^-} \quad (13)$$

$$Sh = \frac{k_M D}{\mathcal{D}_{wo}} = -\frac{D}{C_b - C_i}\frac{\partial C}{\partial r}\Big|_{r=r_i^-} \quad (14)$$

In the boundary layer since heat and mass transfer happen simultaneously, wax concentration is strongly controlled by the temperature.[21] For considering this dependence, a new method was applied, which is called solubility method, to calculated total wax mass flux.

$$Sh \cong \frac{\partial C}{\partial T}\Big|_{r_i}\frac{\Delta T}{\Delta C}Nu \quad (15)$$

The governing equation for solid fraction will remain the same while the equation for thickness will be changed to:

$$-\frac{dr_i}{dt} = \frac{-D_{wo}\frac{dC}{dT}\frac{dT}{dr}\Big|_{r_i^-} + D_e\frac{\partial C}{\partial r}\Big|_{r_i^+}}{\bar{F}_w\rho_{oil}} - \frac{m\tau^n}{2\pi r_i\bar{F}_w\rho_{oil}} \quad (16)$$

where $\frac{dT}{dr}\Big|_{r_i^-}$ is temperature gradient in radial direction at the interface in the oil phase, $\frac{\partial C}{\partial r}\Big|_{r_i^+}$is the concentration gradient in the deposit at the interface in the gel deposit side, τ is shear stress and m and n are fitting parameters that need to be manually adjusted to match the data.[3]

Notably, as we have effective diffusivity in our governing equations (9) and (16), we also have k_α which is the same limiting factor as in laminar flow condition. Therefore, in turbulent flow there are three limiting factors required to be adjusted.

3 METHODOLOGY

3.1 Laminar Flow

Wax concentration will decrease along the test section as some of it will contribute to deposit on the pipe wall. A concentration update is required in calculations.

$$\frac{dC}{dz} = -k_l\left(C_{b_0} - C_i\right) * 2\pi r_i * \frac{\rho_L}{w_h} \quad (17)$$

Equation (17) varies in time and location. Consequently, it has to be measured for each time step for each location. Runge-Kutta method has been used for calculating bulk concentration.

Furthermore, the two governing equations (9) and (10) have been numerically solved simultaneously by Runge-Kutta two variable method using C++ platform while, as part of the RK4 calculations, bulk concentration should be updated for each half/full time step by solving equation (17). This newly applied approach minimizes the possible error since C_b has been updated correctly during calculation of thickness and solid wax fraction.

In Figure 1, the calculation procedure has been illustrated. The first subscription is time and the second one is location. For each section, bulk concentration at the next grid point is calculated from equation (17) using RK4 and the updated bulk concentration is employed in solving equations (9) and (10) by using Runge-Kutta method for that section (interval). In addition, the calculated bulk concentration also uses as one of the three inputs for calculating C_b for the next grid point. Taking into account that the grid points are non-uniform, this procedure will continue till the last section.

In order to match the prediction with experimental data, the fitting parameter needs to be manually adjusted. Since one of the objectives of this research is to understand the potential effects of different factors on K_α, it is not logical to let the fitting parameter be adjusted manually.

Levenberg–Marquardt method[22] was used to do the job to choose the optimal K_α automatically. Therefore, the calculated fitting parameters are going to be more reliable to be analyzed. The main applicability of the Levenberg–Marquardt algorithm is in the least squares curve fitting problem.[23]

$$e_m = y_i - f(x_i, \vec{w}) \quad (18)$$

$$E = \frac{1}{2}\sum_{m=1}^{M} e_m^2 \quad (19)$$

$$g_i = \frac{\partial E}{\partial w_i} = \sum_{m=1}^{m=M}\left(e_m \frac{\partial e_m}{\partial w_i}\right) \quad (20)$$

Newton algorithm gives:

$$g_{1,k+1} = g_{1,k} + \frac{\partial^2 E_k}{\partial w_1^2}\Delta w_1 + \frac{\partial^2 E_k}{\partial w_2 \partial w_1}\Delta w_2 + \cdots + \frac{\partial^2 E_k}{\partial w_n \partial w_1}\Delta w_n$$
$$g_{2,k+1} = g_{2,k} + \frac{\partial^2 E_k}{\partial w_1 \partial w_2}\Delta w_1 + \frac{\partial^2 E_k}{\partial w_2^2}\Delta w_2 + \cdots + \frac{\partial^2 E_k}{\partial w_n \partial w_2}\Delta w_n$$
$$\vdots$$
$$g_{n,k+1} = g_{n,k} + \frac{\partial^2 E_k}{\partial w_1 \partial w_n}\Delta w_1 + \frac{\partial^2 E_k}{\partial w_2 \partial w_n}\Delta w_2 + \cdots + \frac{\partial^2 E_k}{\partial w_n^2}\Delta w_n$$

At the minimum point of the function E, gradient g is zero ($g_{i,k+1} = 0$), and then:

$$-\vec{g} = \begin{bmatrix} -\frac{\partial E_k}{\partial w_1} \\ -\frac{\partial E_k}{\partial w_2} \\ \vdots \\ -\frac{\partial E_k}{\partial w_n} \end{bmatrix} = \begin{bmatrix} \frac{\partial^2 E_k}{\partial w_1^2} & \frac{\partial^2 E_k}{\partial w_2 \partial w_1} & \cdots & \frac{\partial^2 E_k}{\partial w_n \partial w_1} \\ \frac{\partial^2 E_k}{\partial w_1 \partial w_2} & \frac{\partial^2 E_k}{\partial w_2^2} & \cdots & \frac{\partial^2 E_k}{\partial w_n \partial w_2} \\ \vdots & \vdots & \ddots & \vdots \\ \frac{\partial^2 E_k}{\partial w_1 \partial w_n} & \frac{\partial^2 E_k}{\partial w_2 \partial w_n} & \cdots & \frac{\partial^2 E_k}{\partial w_n^2} \end{bmatrix} \begin{bmatrix} \Delta w_1 \\ \Delta w_2 \\ \vdots \\ \Delta w_n \end{bmatrix}$$

$$\vec{w}_{k+1} = \vec{w}_k - \boldsymbol{H}^{-1}\vec{g} \quad (21)$$

The matrix for second order derivative of E_k is called Hessian matrix $\boldsymbol{H}$. Hessian matrix can be replaced by

$$\boldsymbol{H} \cong \boldsymbol{J}^T\boldsymbol{J} \quad (22)$$

Where $\boldsymbol{J}$[24] is a Jacobian matrix And finally we can write:

$$\vec{w}_{k+1} = \vec{w}_k - (\boldsymbol{J}^T\boldsymbol{J} + \mu\boldsymbol{I})^{-1}\boldsymbol{J}^T\vec{e} \quad (23)$$

$$\left(\boldsymbol{J}^T\boldsymbol{J} + \mu\boldsymbol{I}\right)(\vec{w}_k - \vec{w}_{k+1}) = \boldsymbol{J}^T\vec{e} \quad (24)$$

Equation (24) can be solved by Gaussian Elimination method in order to give the optimal $\vec{w}$.

In this paper, our weight (fitting parameter) is k_α and the Levenberg–Marquardt algorithm calculates our limiting factor.

3.1.1 Wax mass flux analysis

After deriving wax fraction and thickness, wax crystal aspect ratios and eventually the fitting parameters will be back calculated based on incoming and aging wax mass flux. The wax mass flux ratio can be calculated from Equation (25) as derived previously in the work of Singh.[25] Later in this paper, equation 25 will be solved by using

central finite difference method using 14400 points from modeling data and will be proven reliable based on obtained results.

$$\frac{j_{age}}{j_{(in)}} = \left(\frac{F_w}{\sigma} * \left(\frac{d\sigma}{dF_w}\right) + 1\right)^{-1} \quad \text{(25)}$$

Also we knew:

$$\frac{j_{age}}{j_{(in)}} = \frac{-D_e \frac{dC}{dr}\Big|_{r_i^+}}{-D_{wo} \frac{dC}{dr}\Big|_{r_i^-}} \quad \text{(26)}$$

$$\frac{j_{age}}{j_{(in)}} = \frac{-D_e \frac{dC}{dr}\Big|_{r_i^+}}{k_M (C_b - C_w)} \quad \text{(27)}$$

From equation (14) we can get k_M:

$$k_M = \frac{Sh * D_{wo}}{2R} \quad \text{(28)}$$

Sherwood number can be written in form:

$$Sh = Nu({}^{Sc}/_{Pr})^{1/3} \quad \text{(29)}$$

From equations (28) and (29) k_M can be written as:

$$k_M = \frac{Nu({}^{Sc}/_{Pr})^{1/3} * D_{wo}}{2R} \quad \text{(30)}$$

Using k_M in equation (30), we rearranged equation (27):

$$\frac{j_{age}}{j_{(in)}} = \frac{-D_e \frac{dc}{dT_i} * \frac{dT}{dr}\Big|_{r_i^+} * 2R}{D_{wo}\left(\frac{Sc}{\mathrm{Pr}}\right)^{\frac{1}{3}} * (C_b - C_i) * \mathrm{Nu}} \quad \text{(31)}$$

Based on equations (11) and (25), we have

$$\left(\frac{F_w}{\sigma} * \left(\frac{d\sigma}{dF_w}\right) + 1\right)^{-1} = \frac{1}{1 + \frac{F_w^2 \alpha^2}{1 - F_w}} * \frac{-\frac{dc}{dT_i} * \frac{dT}{dr} * 2 * R}{\left(\frac{Sc}{\mathrm{Pr}}\right)^{\frac{1}{3}} * (C_b - C_i) * \mathrm{Nu}} \quad \text{(32)}$$

The left hand side of the equation (32) has been solved using central finite difference method from obtained modeling results. From this equation (32) wax crystal aspect ratio can be back calculated. The results are discussed in the following sections.

3.2 Turbulent Flow

The wax mass flux calculation approaches for turbulent and laminar flow are similar. Venkatesan model assumes that the concentration profile is completely controlled by the temperature profile (or the instantaneous precipitation occur). Thus, k_M is calculated from:

$$q_{M,IN} = k_M (C_b - C_i) = -\mathcal{D}_{wo} \frac{dc}{dT} \frac{dT}{dr}\Big|_{r_i^-} \quad \text{(33)}$$

$$\frac{dT}{dr}\Big|_{r_i^-} = -Nu * \frac{(T_b - T_i)}{D} \quad \text{(34)}$$

where, $q_{M,IN}$ is the total mass wax flux, C_b is the bulk concentration, C_i is concentration at the interface, $\mathcal{D}_{wo}$ is molecular diffusivity and $\left.\frac{dT}{dr}\right|_{r_i^-}$ is the temperature gradient at the interface in the oil side. By simultaneously solving the equations (9) and (16), the thickness and solid fraction can be predicted.

4 RESULT AND DISCUSSION

The theoretical procedure has been fully elaborated. At this section, the numerical approach has been implemented and the results are presented and analyzed.

4.1 Laminar flow

For laminar flow, the new approach has been employed and the results have been compared with experimental data as well as with Singh et al.[1] prediction.

4.1.1 Modeling accuracy and error

With data available for five cases[1] (Table 1), the solid wax fractions were almost the same for both modeling approaches while the accuracy for r_i/R terms were different for the initial time range. The proposed model, shown in in this paper, has error less than Singh prediction almost in all cases for $t_{day} = [0\ ,1]$, graphically shown in Figure 3.

In the following section, the prediction and experimental data have been compared. It can be noticed, in the figures 4-7 bellow for all 5 cases with different ambient temperatures and flow rates, the deposit thickness model exactly matched with experimental data. Modeling data for cases Q=1 $\frac{Gallon}{min}$ with Ta = 8.2℃, 7.3℃ and 4.4℃ and also case Q=2.5 $\frac{Gallon}{min}$ with Ta=8.3℃ almost with 100% accuracy repeats experimental data especially at initial time range. However, for the case Q=4 $\frac{Gallon}{min}$ and Ta = 8.9℃, at the beginning of the time period, there is a little gap between experimental data and the model, but the difference is rather negligible

In Figure 9, wax thickness versus wax fraction pattern was analyzed and compared to experimental data. The experimental data were rearranged to this illustrated form from already given experimental data. In the graph, interpolated experimental data start from the first given experimental points. The model almost repeats the same pattern. However since experimental data were not available at initial times, no judgment can be made for the modeling curves at that time interval.

4.1.2 Fitting Parameter

In this section, the fitting parameters K_α have been investigated. Two elements affecting K_α include volumetric flow rates and ambient temperature. In the table 2, the corresponding K_α(calculated by LM method) for each case has been shown. In Figure 10, the corresponding K_α for each case has been illustrated from back calculation from equation (32). Notably, for very early times, the linear relationship between wax crystal aspect ratio and wax fraction is not seen. However, for the rest, calculated K_α(s) show acceptable agreements with the original ones (form LM).

In summary, from Table 2 and Figure 10, it can be noticed that "α" decreases as flow rate increases. Also, with assuming constant flow rate, k_α increases as temperature stars to decrease (figure 10). The final wax crystal aspect ratios and their comparisons with Singh et al has been included in figure 11.

4.2- Turbulent flow

In turbulent flow, the governing equations will be influenced by sear stress as flow rate is high. Equations (16) and (9) have been simultaneously calculated while three fitting parameters needed to be adjusted by matching the results from modeling to experimental data. In figure (12) and (13), the best fitted models have been shown and the corresponding fitting parameters are shown in table 3.

5 CONCLUSION

The experimental data from Singh et al[1] and Venkatesan[3] are analyzed in this study. The implementation of RK4 in solving the transport equations are improved by adding the heat transfer and the overall mass balance in each intermediate step of RK4 calculation. Moreover, the axial concentration along the pipe is not assumed to be constant. The additional mass balance equation was added to calculate the bulk concentration at each location, instead of using the bulk concentration at the inlet as the representative of the local bulk concentration. The direct finding from this study is that K_α (the slope between the wax crystal aspect ratio and wax fraction) increases as flow rate decreases. The obtained final wax crystal aspect ratio based on the modeling approach is lower than the value reported in Singh et al work. This indicate that the final wax crystal aspect ratio from the model may not be unique and can be dependent upon the way that the numerical method is implemented.

The linear relationship between the K_α and the flow rate was found. This result shows that the slope of the wax crystal aspect ratio with wax fraction (not the wax crystal aspect ratio itself) can be used as the preliminary closure relationship for predicting the α in wax deposition model. The result from this study also suggests that more laminar flow data are needed for developing the comprehensive closure relationship for predicting wax deposition in laminar flow. Last but not least, the closure relationship of the wax crystal aspect ratio can be sensitive to the way that engineers and scientist implement the numerical method. The standard open-source software, if available, can facilitate the modeling of this closure relationship among researcher significantly.

6 REFERENCE

(1) Singh, P.; Venkatesan, R.; Fogler, H. S.; Nagarajan, N. Formation and Aging of Incipient Thin Film Wax-Oil Gels. *AIChE Journal* **2000**, *46*, 1059–1074.

(2) Aske, N.; Kallevik, H.; Sjöblom, J. Determination of Saturate, Aromatic, Resin, and Asphaltenic (SARA) Components in Crude Oils by Means of Infrared and near-Infrared Spectroscopy. *Energy and Fuels* **2001**, *15*, 1304–1312.

(3) Venkatesan, R. *The Deposition and Rheology of Organic Gels*; Ph.D. dissertation, The University of Michigan, Ann Arbor, Michigan, 2004.

(4) Lee, H. S. H. S. *Computational and Rheological Study of Wax Deposition and Gelation in Subsea Pipelines*; Ph.D. dissertation, The University of Michigan, Ann Arbor, Michigan, 2008.

(5) Coutinho, J. a. P.; Daridon, J.-L. The Limitations of the Cloud Point Measurement Techniques and the Influence of the Oil Composition on Its Detection. *Petroleum Science and Technology* **2005**, *23*, 1113–1128.

(6) Bott, T. Aspects of Crystallization Fouling. *Experimental Thermal and Fluid Science* **1997**, *14*, 356–360.

(7) Moritis, G. Flow Assurance Challenges Production from Deeper Water. *Oil and Gas J.* **2001**, *99*, 66.

(8) Svendsen, J. J. A. Mathematical Modeling of Wax Deposition in Oil Pipeline Systems. *AIChE Journal* **1993**, *39*, 1377–1388.

(9) Majeed, A.; Bringedal, B.; Overa, S. Model Calculates Wax Deposition for N. Sea Oils. *Oil & Gas Journal* **1990**, *88*, 63–69.

(10) Burger, E.; Perkins, T.; Striegler, J. Studies of Wax Deposition in the Trans Alaska Pipeline. *Journal of Petroleum Technology* **1981**, *33*, 1075–1086.

(11) Ribeiro, F. S.; Souza Mendes, P. R.; Braga, S. L. Obstruction of Pipelines due to Paraffin Deposition during the Flow of Crude Oils. *International Journal of Heat Mass Transfer* **1997**, *40*, 4319–4328.

(12) Labes-Carrier, C.; Rønningsen, H. Wax Deposition in North Sea Gas Condensate and Oil Systems: Comparison between Operational Experience and Model Prediction. In *SPE Annual Technical Conference and Exhibition, 29 September-2 October, San Antonio, Texas*; 2002; p. SPE – 77573 – MS.

(13) Huang, Z.; Lee, H. S.; Senra, M.; Fogler, H. S. A Fundamental Model of Wax Deposition in Subsea Oil Pipelines. *AIChE Journal* **2011**, *57*, 2955–2964.

(14) Panacharoensawad, E.; Sarica, C. Wax Deposit Surface Characteristic under Single-Phase and Water-in-Crude-Oil Flow Conditions. In *Offshore Technology Conference, 5-8 May, Houston, Texas*; Offshore Technology Conference, 2014; p. OTC – 25097 – MS.

(15) Rittirong, A. *Paraffin Deposition Under Two-Phase Gas-Oil Slug Flow in Horizontal Pipes*; Ph.D. dissertation, The University of Tulsa, Tulsa, Oklahoma, 2014.

(16) Cussler, E. L.; Hughes, S. E.; Ward, W. J.; Aris, R. Barrier Membranes. *Journal of Membrane Science* **1988**, *38*, 161–174.

(17) Ashbaugh, H. H. S.; Radulescu, A.; Prud'homme, R. K.; Schwahn, D.; Richter, D.; Fetters, L. J. Interaction of Paraffin Wax Gels with Random Crystalline/Amorphous Hydrocarbon Copolymers. *Macromolecules* **2002**, *35*, 7044–7053.

(18) Hayduk, W.; Minhas, B. S. Correlations for Prediction of Molecular Diffusivities in Liquids. *Canadian Journal of Chemical Engineering*, 1982, *60*, 295–299.

(19) Mehrotra, A. K.; Bhat, N. V; Tn, C. Modeling the Effect of Shear Stress on Deposition from " Waxy " Mixtures under Laminar Flow with Heat Transfer. *Energy & fuels* **2007**, 1277–1286.

(20) Venkatesan, R.; Nagarajan, N. R.; Paso, K.; Yi, Y. B.; Sastry, A. M.; Fogler, H. S. The Strength of Paraffin Gels Formed under Static and Flow Conditions. *Chemical Engineering Science* **2005**, *60*, 3587–3598.

(21) Venkatesan, R.; Fogler, H. S. Comments on Analogies for Correlated Heat and Mass Transfer in Turbulent Flow. *AIChE Journal* **2004**, *50*, 1623–1626.

(22) Yu, H.; Wilamowski, B. M. Levenberg-Marquardt Training. *Industrial Electronics Handbook, vol. 5 – Intelligent Systems* **2011**, 12–1 to 12–18.

(23) Ranganathan, A. The Levenberg-Marquardt Algorithm http://users-phys.au.dk/jensjh/numeric/project/10.1.1.135.865.pdf.

(24) Menhaj, M. T. Ha. and M. B. Training Feedfoward Networks with the Marquardt Algorithn. *Neural Network, IEEE Transaction* **1994**, *5*, 989–993.

(25) Singh, A. *Experimental and Field Verification Study of Wax Deposition in Turbulent Flow Conditions*; M.S. Thesis, The University of Tulsa, Tulsa, Oklahoma, 2013.

Table 1 - Summary of experimental database for single phase wax deposition.

Data sourse	Case number	Pipe ID, cm	μ_{oil}, Pa-s	ρ_{oil}, kg/m3	T_{bulk}, °C	t_{test}, days	$T_{ambient}$, °C	Q, gal/s
Singh et al (Laminar flow)	1	1.44	0.0087	838.5	22.2	5	8.3	1.00
	2						8.3	2.50
	3						8.9	4.00
	4						7.2	1.00
	5						4.4	1.00
Venkatesan (Turbulent flow)	1	2.225	0.00412	838.5	25.556	0.85	4.444	10.0
	2							15.0
	3							20.0
	4							25.0

Table 2 - Corresponding K_α for laminar flow.

$T_{ambient}$, [°C]	Q, [gal/min]	K_α
8.3	1.0	98.8
8.3	2.5	31
8.9	4.0	20.2
7.2	1.0	107
4.4	1.0	146.3

Table 3 – Corresponding fitting parameters for turbulent flow

$T_{ambient}$, [°C]	Q, [gal/min]	K_α	n	m
4.44	10.0	460	2.15	2.84×10^{-9}
	15.0	500	1.909	2.0×10^{-9}
	20.0	550	2.1	6.5×10^{-9}
	25.0	610	2.47	9.8×10^{-9}

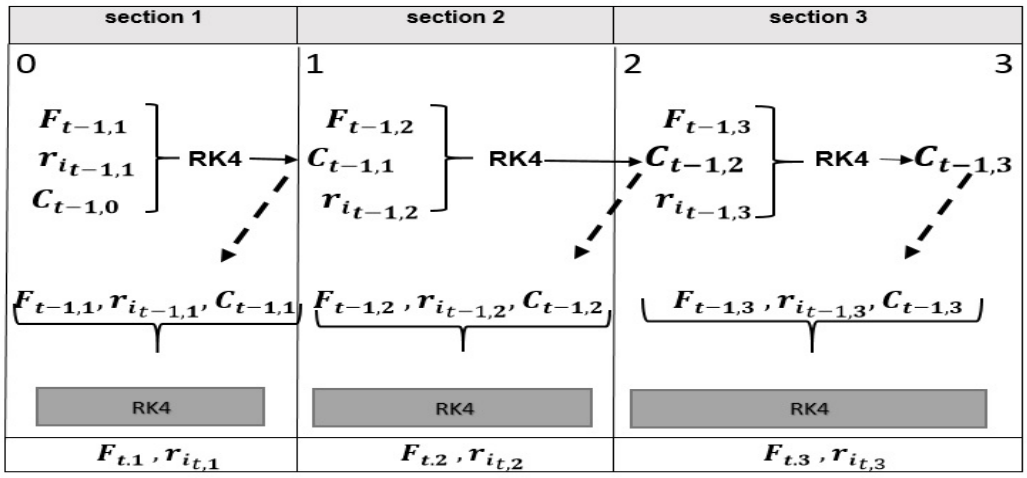

Figure 1 - Calculation Procedure.

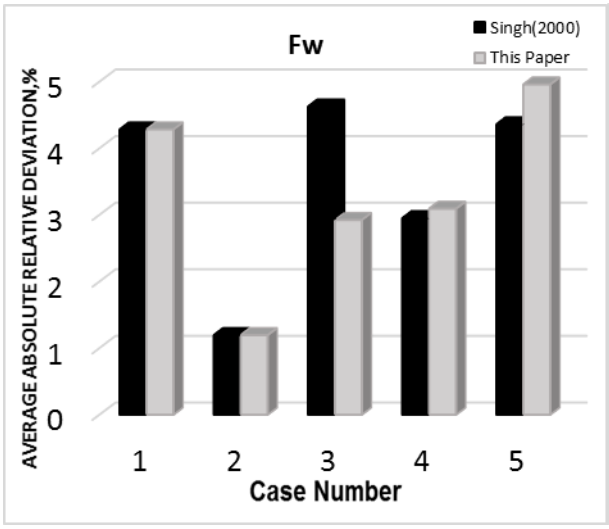

Figure 2 - Comparison for F_w term for t= [0.4, 5].

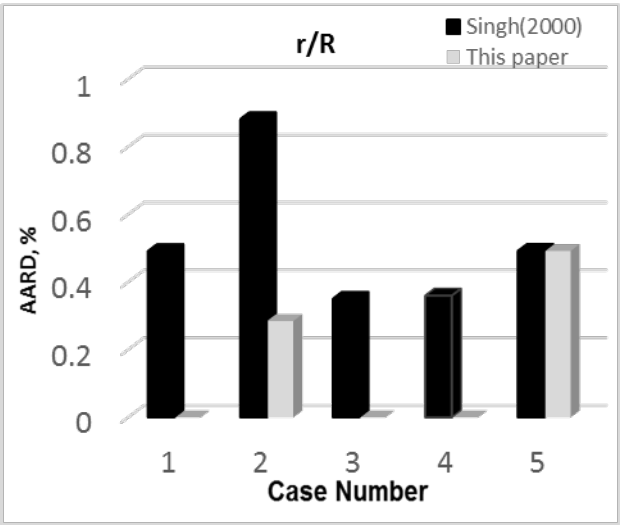

Figure 3 - Comparison for r_i/R term for t= [0, 1].

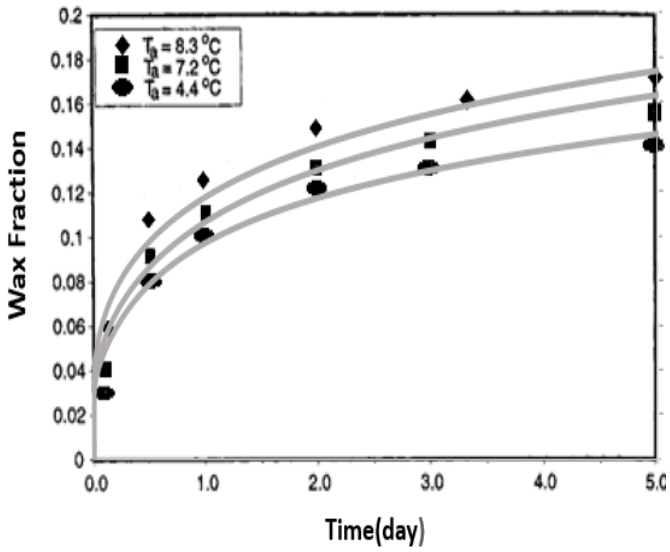

Figure 4 - Experimental vs proposed modeling data.

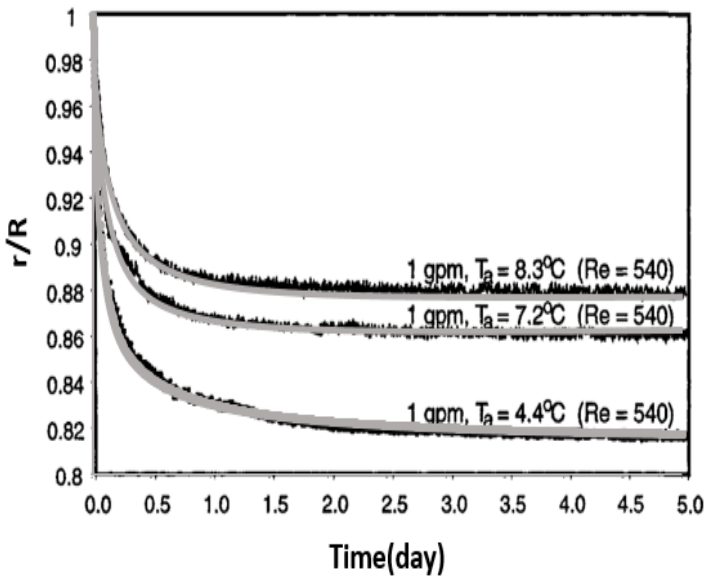

Figure 5 - Experimental vs proposed modeling data

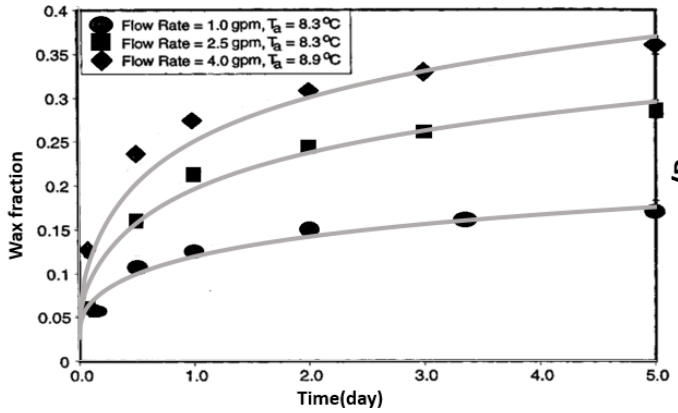

Figure 6 – Exp. vs modeling data for wax fraction

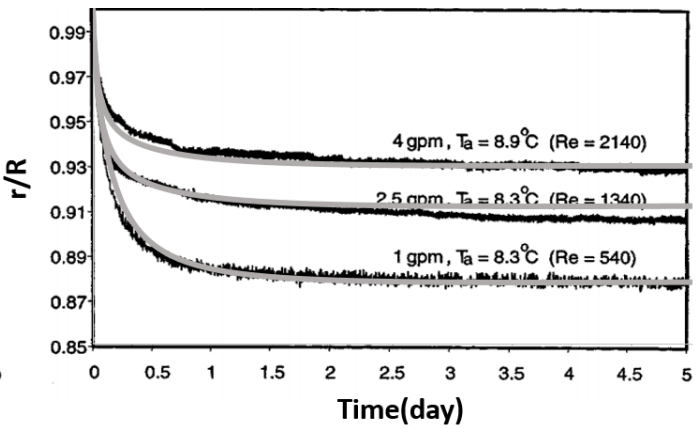

Figure 7 – Exp. vs modeling data for effective radius.

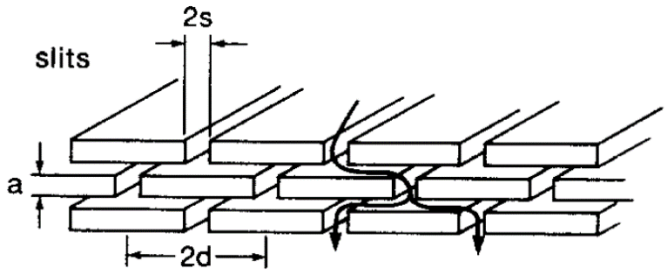

Figure 8 - Slits model.[16]

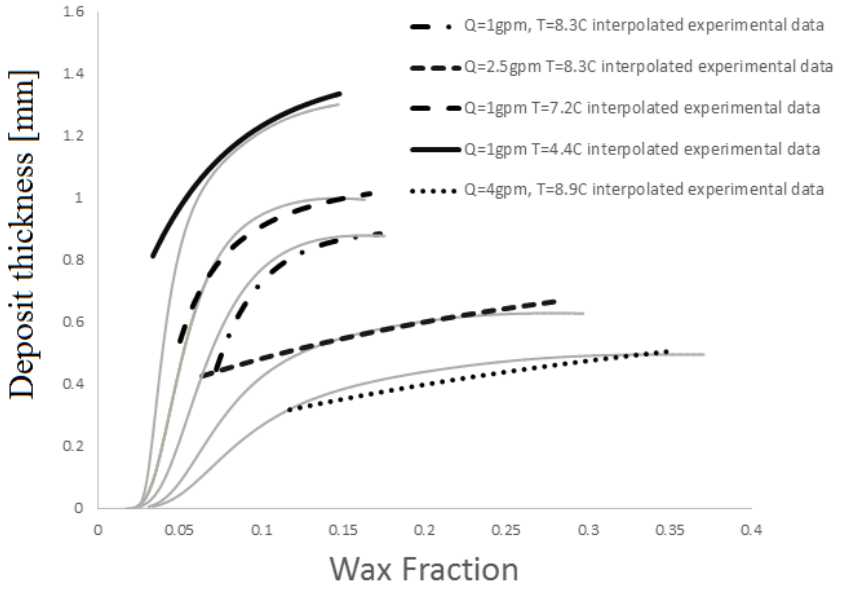

Figure 9 – Comparison between modeling and interpolated experimental data for laminar flow.

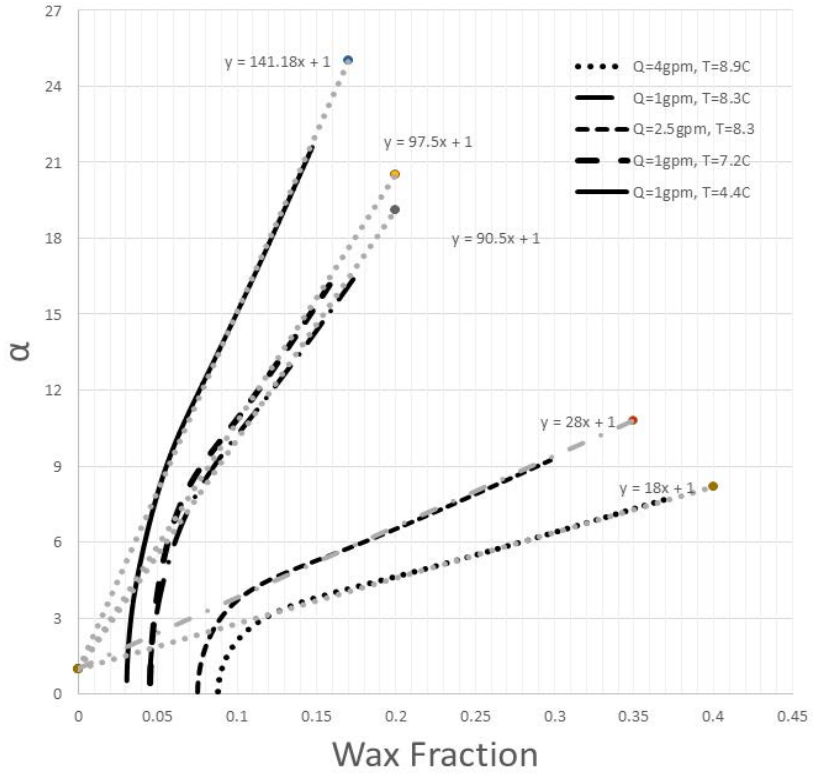

Figure 10 – Wax crystal aspect ratio versus wax fraction from back calculation.

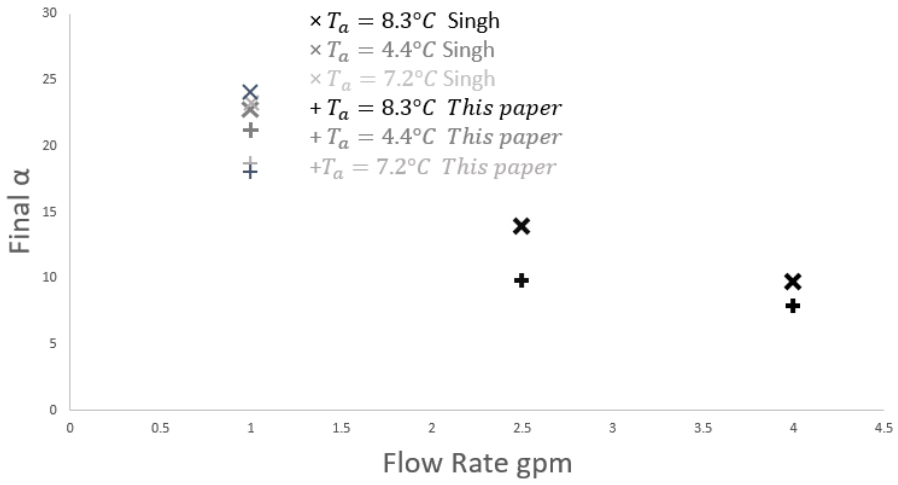

Figure 11 – Final Wax crystal aspect ratio comparison with Singh et al.[1]

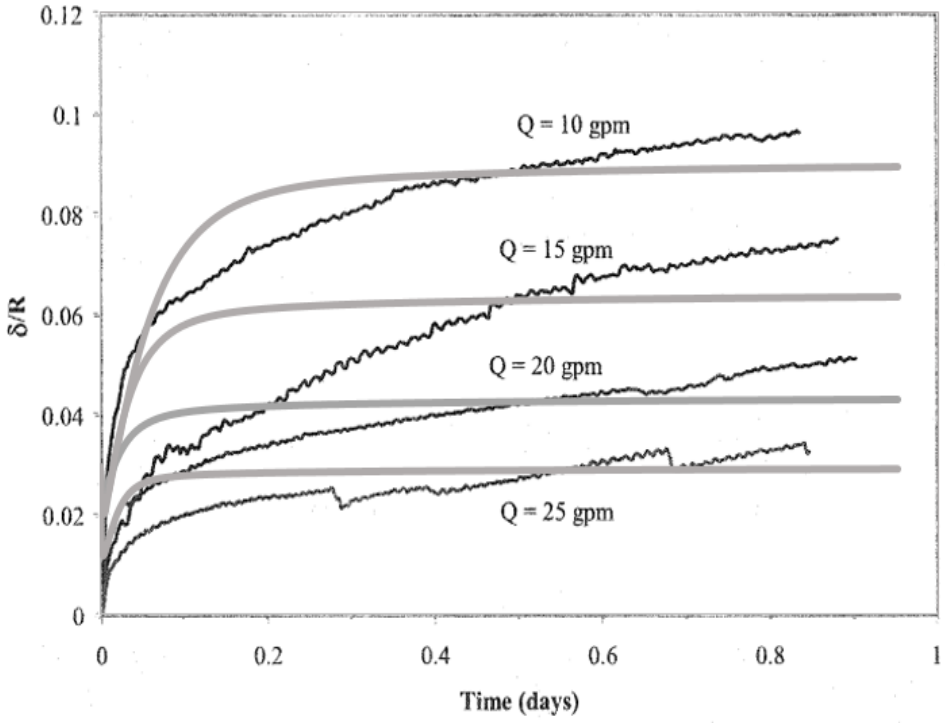

Figure 12– Modeling versus Venkatesan experimental data

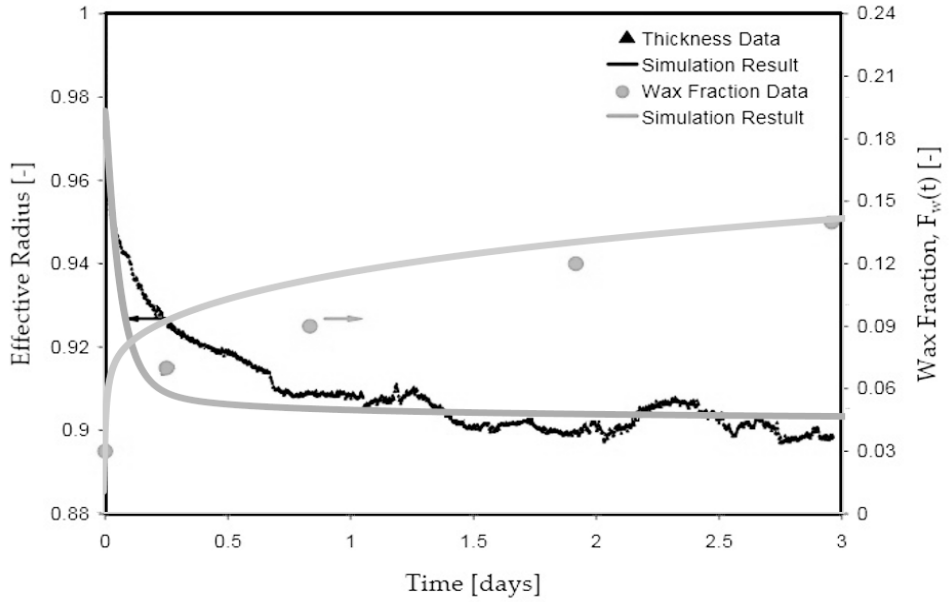

Figure 13 – Wax fraction and effective radius for Q=10 gpm for turbulent flow.

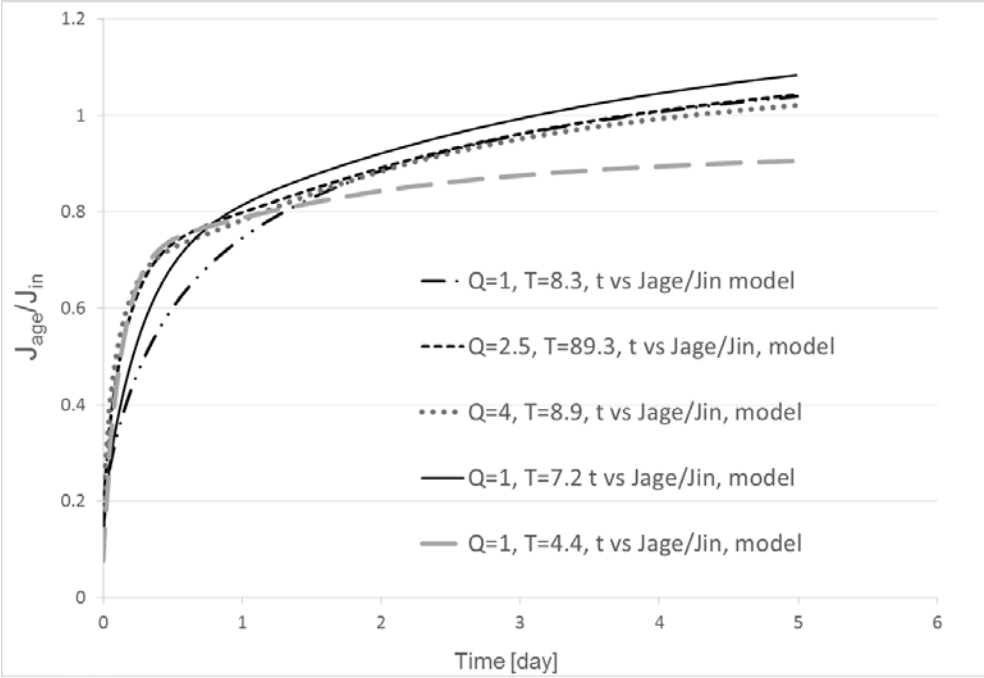

Figure 14 - The wax mass flux ratio for laminar flow cases where aging ratio increases with time.

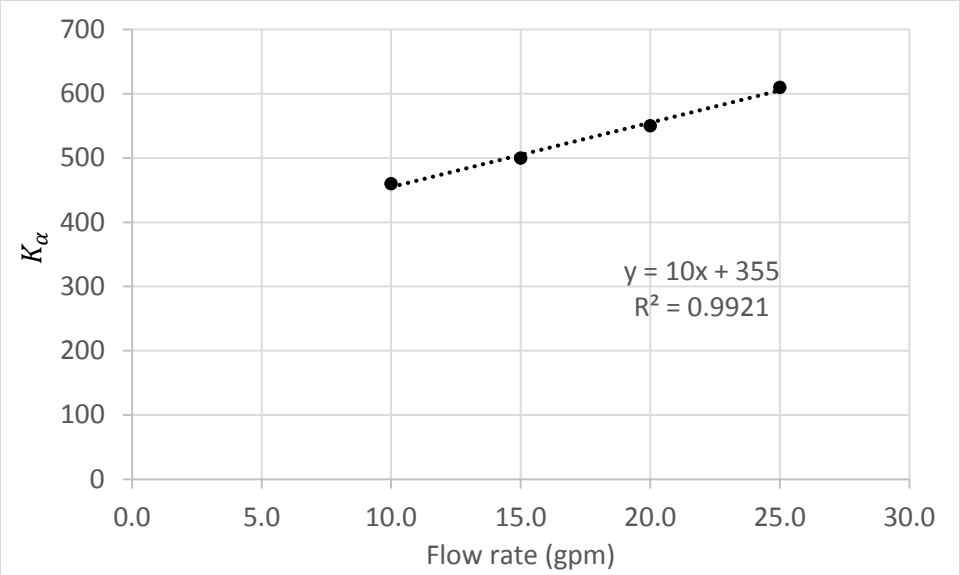

Figure 15 - The slope between the wax crystal aspect ratio and flow rate for turbulent flow case (based on Venkatesan data[3])